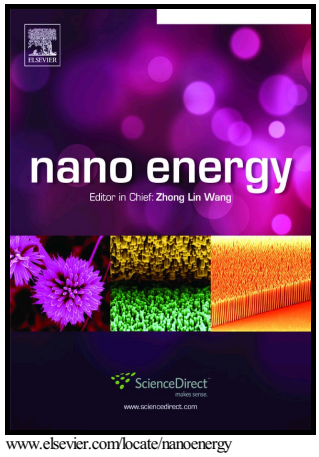

www.elsevier.com/locate/nanoenergy

Embellished Hollow Spherical Catalyst Boosting Activity and Durability for Oxygen Reduction Reaction

Pan Xu, Jing Zhang, Gaopeng Jiang, Fathy Hassan, Ja-Yeon Choi, Xiaogang Fu, Pouyan Zamani, Lijun Yang, Dustin Banham, Siyu Ye, Zhongwei Chen

PII: S2211-2855(18)30519-6
DOI: https://doi.org/10.1016/j.nanoen.2018.07.031
Reference: NANOEN2898

To appear in: *Nano Energy*

Received date: 21 May 2018
Revised date: 12 July 2018
Accepted date: 13 July 2018

Cite this article as: Pan Xu, Jing Zhang, Gaopeng Jiang, Fathy Hassan, Ja-Yeon Choi, Xiaogang Fu, Pouyan Zamani, Lijun Yang, Dustin Banham, Siyu Ye and Zhongwei Chen, Embellished Hollow Spherical Catalyst Boosting Activity and Durability for Oxygen Reduction Reaction, *Nano Energy,* https://doi.org/10.1016/j.nanoen.2018.07.031

Embellished Hollow Spherical Catalyst Boosting Activity and Durability for Oxygen Reduction Reaction

Pan Xu[a,1], *Jing Zhang*[a,1], *Gaopeng Jiang*[a], *Fathy Hassan*[a], *Ja-Yeon Choi*[a,b], *Xiaogang Fu*[a], *Pouyan Zamani*[a], *Lijun Yang*[b], *Dustin Banham*[b], *Siyu Ye*[b], *Zhongwei Chen**[a]

[a]Department of Chemical Engineering, Waterloo Institute for Nanotechnology, University of Waterloo, 200 University Ave. W, Waterloo, ON, N2L 3G1, Canada

[b]Ballard Power Systems, 9000 Glenlyon Parkway, Burnaby, BC, V5J 5J8, Canada

*Corresponding author: E-mail: zhwchen@uwaterloo.ca

ABSTRACT

Transition metals hybridized to heteroatom doped carbon material can be regarded as the most promising non-noble candidate for boosting the sluggish kinetics of oxygen reduction reaction (ORR). However, it has always been a challenge to vastly boost the activity, and simultaneously retain a favorable structure from the supporting material. Herein, we prepared a high surface area hollow spherical carbon as a supporting material, and employed aminothiophenol (ATI) and poly-aminothiophenol (PATI) as heteroatom precursors to synthesize nitrogen and sulfur co-doped catalysts, i.e. HCS-A and HCS-PA, respectively. The two catalysts possessed chemically similar surface composition, and nearly identical chemical states for each element. However, only HCS-A was able to vastly inherit both morphological advantage and high surface area from the carbon support. In further half-cell electrochemical testing, HCS-A performed better ORR activities and higher selectivity toward 4 electron pathway than HCS-PA in both acidic and

[1] The authors contributed equally to this work

alkaline media. Moreover, HCS-A was proven to have excellent durability in half-cell testing, methanol tolerance as well as outstanding peak power density in both fuel cells and zinc-air batteries. This work not only indicates the promising performances of HCS-A, but more importantly offers a new viewpoint on the selection of heteroatom precursor to retain a favorable structure.

Graphical abstract

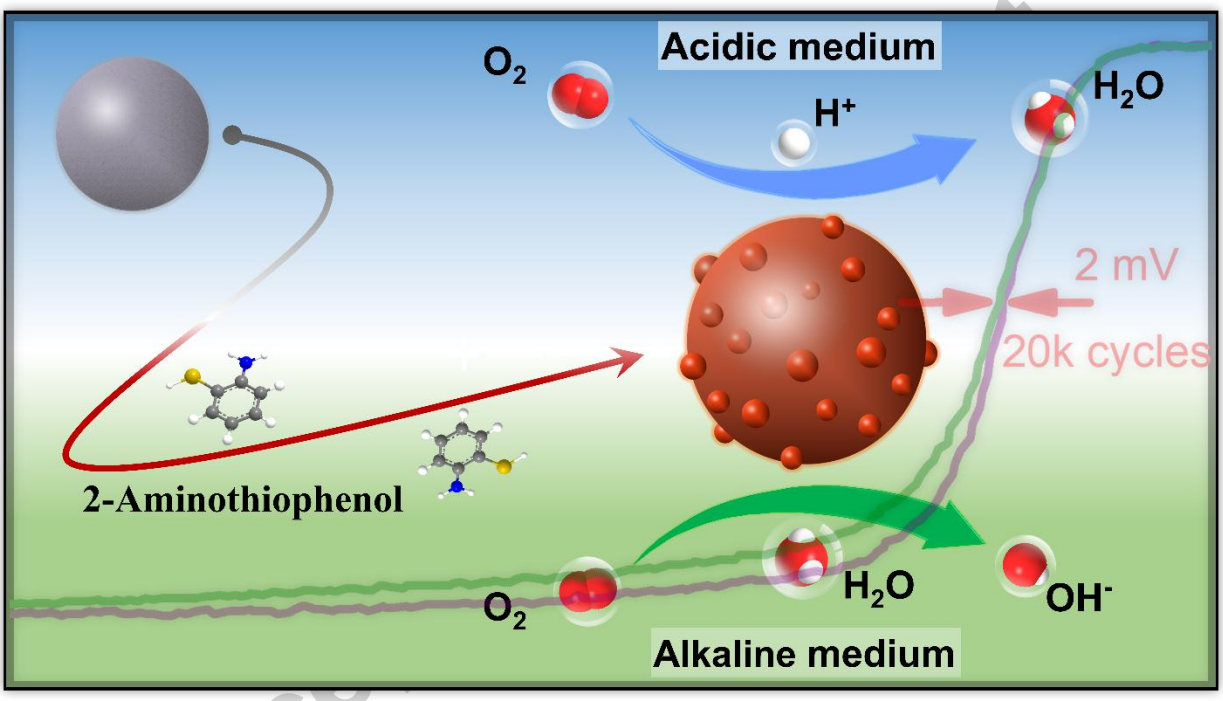

Embellished hollow carbon spherical NPM catalyst (i.e. HCS-A) was synthesized to boost oxygen reduction reaction in both acidic and alkline media. The resultant catalyst shows excellent activity and durability.

KEYWORDS

Hollow sphere; Oxygen reduction; Non-precious catalyst; Electron transfer number; PEM Fuel Cell; Zinc-air battery.

1. INTRODUCTION

Increasing consumption of energy and rising rate of carbon dioxide emissions have caused the twin challenges of energy shortage and climate change. To address these problems, researchers have developed various electrochemical technologies including fuel cells [1], lithium ion batteries [2], metal-air batteries [3], metal-sulfur batteries [4], flow batteries [5], and so on. In principle, these electrochemical devices generate electricity through the integration of two separate half-reactions. For fuel cells and metal-air batteries with the air electrodes, the oxygen reduction reaction (ORR) is the crucial half-reaction that limits overall power performance [6]. In order to overcome the sluggish kinetics of the oxygen reduction reaction, a catalyst accelerating the ORR process is essential at the air electrode. Up to now, platinum group metal based electrocatalysts are the most active and stable catalysts for ORR. However, the widespread use of these precious metals is impeded by the high cost and limited reserves. A considerable alternative is to search for cost-effective and earth-abundant non-precious metal catalysts (NPMCs).

Along with the development of NPMCs, the understanding of their ORR active sites has been evolving over the past few decades. To date, some scientists think that transition metals are directly involved in the active sites by metal-nitrogen coordination [7-9]. On the other hand, some others believe that the active sites stay in the carbon and nitrogen frameworks, and transition metals only catalyze the formation of these active sites [10, 11]. Even though the academia holds different opinions on the nature of active sites, it is conclusive that the NPMCs prepared with transition metals are superior to the transition metal free catalysts, especially in an acidic medium. One of the joint efforts made by scientists in the past few decades is to find proper precursors to achieve higher electrocatalytic activity. Metal-N_x chelate was initially proven to be ORR active [12], and then pyrolyzed non-macrocyclic material demonstrated high

activity towards ORR several years later [13]. Since the precursors shifted from macrocyclic material to non-macrocyclic material, many varieties of nitrogen precursors have emerged in recent years [14-16], as well as other types of heteroatom (boron, sulfur, phosphorus, etc.) doping and dual doping precursors [17, 18]. An additional heteroatom dual doping is believed to not only increase the active site density but also the activity of the active sites [19]. When selecting heteroatom precursors, researchers normally focus on factors like heteroatom content and molecular configuration, but little attention has been paid to the effect of molecular size. Although many different monomers and polymers have been used individually as heteroatom precursors in numerous researches, no work has been done to specifically study the difference between a monomer and its polymer as heteroatom precursors. Therefore, considering the component similarity and the molecular size imparity between a monomer and its polymer, it is worthwhile to investigate the similarities and differences between the two types of catalyst derived from monomers and their polymer counterparts, respectively.

Therefore, inspired by the discussion above, we have designed NPMCs which are heat-treated composites of an iron precursor together with poly(aminothiophenol) (PATI) and its monomer aminothiophenol (ATI), respectively. Particularly, ultra-high surface area nitrogen-doped hollow carbon spheres (HCS) was successfully achieved for supporting the catalytically active materials. The spherical morphology was purposely targeted because the void spaces among the spheres are sufficient for oxygen permeation, and the ultra-high surface area allows the catalyst to carry more accessible active sites. Accordingly, several interesting findings were observed for HCS-supported Fe-N/C catalyst derived from ATI (HCS-A) compared to the catalyst derived from PATI (HCS-PA). Firstly, HCS-A is able to maintain the hollow spherical structure and high surface area from activated HCS, while HCS-PA transforms into large carbon particles

coexisting with carbon spheres and sacrifices most of the surface area. Secondly, elemental surface composition and chemical states of each element are quite similar for HCS-A and HCS-PA, indicating that similar chemical bonding and active sites was formed. Thirdly, HCS-A shows better ORR activity than HCS-PA in terms of both kinetic and mass transport processes.

2. MATERIALS AND METHODS

Preparation of activated hollow carbon sphere (HCS): Firstly, polyaniline-co-polypyrrole nano spheres were synthesized though emulsion polymerization method with Triton X-100 as the surfactant [20, 21]. The obtained co-polymer was pre-carbonized at 400 ^{o}C to get HCS. After that, the HCS was mixed with KOH at a mass ratio of 1:3. The mixture was heated to 800 ^{o}C under the protection of argon at a ramp rate of 5 ^{o}C/min and held for 1 hour to get activated HCS. The activated HCS was then washed with DDI to neutral PH and dried in a vacuum oven for later use.

Preparation of HCS-PA: In a typical protocol, 120 mg 2-aminothiophenol and 20 mg ferrous acetate was dissolved in 20ml ethanol, respectively. The 2-aminothiophenol solution was added to the ferrous acetate solution dropwise with vigorous stirring. Then, a certain amount of ammonium persulphate solution was added. The mixed solution was heated to 60 ^{o}C to allow polymerization. After polymerizing for 8 hours, 60 mg activated HCS powder was added to the solution. After 1 hour of sonication and stirring overnight, the mixture was dried at 80 ^{o}C and grinded into fine powder. HCS-PA was obtained after pyrolysis of the dry powder at 900 ^{o}C for 1 hour.

Preparation of HCS-A: In a typical protocol, 120 mg 2-Aminothiophenol and 20 mg ferrous acetate was dissolved in 20ml ethanol, respectively. The 2-aminothiophenol solution was added

to the ferrous acetate solution dropwise with vigorous stirring. The mixed solution turned black after 2-aminothiophenol was added and from back to brown after stirring for several minutes. Then, 60 mg activated HCS powder was added to the solution. After sonication for 1 hour and stirring overnight, the mixture was dried at 80 ^{o}C and ground into a fine powder. HCS-A was obtained after pyrolysis of the dry powder at 900 ^{o}C for 1 hour.

Physicochemical characterizations: The catalyst morphology was investigated by scanning electron microscopy (SEM) with a LEO FESEM 1530 microscope, and transmission electron microscopy (TEM) with a JEOL 2010F TEM/STEM field emission microscope. Brunauer-Emmett-Teller (BET) surface area was measured by the nitrogen adsorption and desorption technique through a Micromeritics ASAP 2010M system. X-ray photoelectron spectroscopy (XPS) was performed with a Thermal Scientific K-Alpha XPS spectrometer to collect the elemental composition of the catalyst materials.

Electrochemical measurements: RDE and RRDE measurements were performed using a CHI Electrochemical Station (Model 750b) in a standard three-electrode cell. For RDE, a 5.0 mm diameter glassy carbon disk (disk geometric area 0.196 cm^2) was used. The RRDE has an extra Pt electrode with inner diameter and outer diameter of 6.5 mm and 7.5 mm (ring geometric area 0.110 cm^2). To avoid any potential contamination of the catalyst by Pt, all experiments were carried out with a graphite rod as a counter electrode. Ag/AgCl (filled with 3M KCl) electrode and SCE electrode were used as the reference electrode in acidic medium (0.5 M H_2SO_4) and alkaline medium (0.1 M KOH), respectively. All potentials initially measured against the Ag/AgCl electrode and SCE electrode were converted to a RHE scale. The catalyst ink was prepared by adding 5 mg of the catalyst to 1 ml isopropanol and ultrasonically blending for 30 min. 20 µl of the ink and 3 µl of 0.25 wt.% Nafion solution was applied to the 0.196 cm^2 disk in

sequence, resulting in a catalyst loading of ca. 0.5 mg cm^{-2}. RDE polarization plots were recorded in both O_2-saturated and N_2-saturated electrolyte at a scan rate of 5 mV s^{-1}. The results shown in this paper have subtracted the N_2 background. RDE cycling stability tests of the HCS-A catalyst were performed in N_2-saturated electrolyte in the potential range from 0.6 to 1.0 V at room temperature. The RRDE collection efficiency N was measured using the reversible $[Fe(CN)_6]^{4-}/[Fe(N)_6]^{3-}$ system. The electrolyte was deaerated 0.1 M KCl with 0.01 M $K_3Fe(N)_6$ and the electrode was rotated under the rotation rates of 400, 900, 1600, and 2500 rpm. Disk potential (E_d) was scanned from 0.8 V to 0.1 V vs. RHE at a scan rate of 10 mV s^{-1} to reduce $[Fe(N)_6]^{3-}$ to $[Fe(CN)_6]^{4-}$. The ring was set at a constant potential (E_r) of 1.5 V vs. RHE to oxidize $[Fe(CN)_6]^{4-}$ back to $[Fe(N)_6]^{3-}$. The collection efficiency can be determined by I_d and I_r: $N = - I_r/I_d$. The collection efficiency remains a constant value of 0.28 ± 0.2 under various ω.

Fuel cell testing: HCS-A catalyst was tested in the fuel cell cathode to evaluate its activity under PEMFC operating conditions. The catalyst ink was prepared by ultrasonically mixing the catalyst powder with Nafion suspension for 1 hour. Then, the catalyst "ink" was brush-painted to the gas diffusion layer (GDL, 29 BC, Ion Power) until the cathode catalyst loading reached ca. 4 mg cm^{-2}. The Nafion content in the catalyst layer was maintained at ca. 35 wt%. Commercial Pt deposited carbon cloth GDE (0.2 mg cm^{-2} Pt, Fuel Cell Etc) was used at the anode. The cathode and anode were hot-pressed onto two sides of a Nafion® 211 membrane to form a three-layer membrane-electrode assembly (MEA). The geometric MEA area was 5.0 cm^2. Fuel cell testing was carried out in a single cell with serpentine flow channels. Pure hydrogen and oxygen, humidified at 80°C, were supplied to the anode and cathode at a flow rate of 200 sccm. Both electrodes were maintained at the same absolute pressure of 20 psig. Fuel cell polarization plots were recorded using fuel cell test stations (Scribner 850e).

Zinc-air battery testing: The single-cell battery was tested using a home-made practical zinc-air battery and a multichannel potentiostat (Princeton Applied Research, VersaSTAT MC) at room temperature. A polished zinc plate (Zinc Sheet EN 988, OnlineMetals) and gas diffusion layer (GDL, ELAT LT 1400W, E-TEK) sprayed with the HCS-A loading of ca. 2 mg cm^{-2} were used as the anode and cathode, respectively. The cathode was exposed to completely ambient air with no O_2 pre-bubbling or continuous O_2 supply. A microporous membrane (25 μm polypropylene membrane, Celgard 5550) and 6.0 M KOH were used as the separator and electrolyte, respectively. The area of the active material layer exposed to the electrolyte and ambient air was 0.785 cm^2.

3. RESULTS AND DISCUSSION

3.1. Physicochemical Characterization

The catalyst preparation process is shown in Fig. 1. Hollow carbon sphere (HCS) structure was first prepared by pre-carbonization of the polyaniline-co-polypyrrole copolymer, followed by KOH etching to obtain activated HCS with ultra-high surface area (Fig. 1a). In order to obtain a highly active ORR catalyst, we used Poly-aminothiophenol (PATI), a sulfur-containing analog of polyaniline, as the heteroatom precursor, ferrous acetate as the metal precursor and HCS as carbon support to prepare the final HCS-PA catalyst (Fig. 1b). As a result, PATI agglomerated and destroyed the uniform structure of HCS. Then, we tried another strategy by using aminothiophenol (ATI) as the heteroatom precursor to prepare HCS-A with the same synthesis procedure (Fig. 1c). Catalyst morphology, surface area, and surface composition were further characterized to study HCS-A and HCS-PA, and conclude the factors that contribute to the ORR activity.

The pre-carbonized HCS exhibited well-defined spherical morphology with a uniform particle size distribution as shown in SEM images (Fig. 2a). When we look at the TEM images (Fig. 2b and Fig. S1), a highly organized hollow structure with a uniform shell thickness can be observed. The outer and inner diameters of the hollow sphere are ca. 110 nm and 60 nm, respectively. After KOH activation at 800 ^{o}C, most of the HCS spheres were able to maintain their spherical structure (Fig. S2). Additionally, small wrinkles can be observed on the edge of the spheres, indicating that the surface layer has been etched during activation. It is also found that some of the spheres were broken, becoming open shell spheres, which exposes the inner surface. As KOH activation is a well-established method to produce micro pores [22], the holes which are large enough to penetrate the shell were probably created by agglomerated KOH particles during high temperature treatment.

From Fig. 2c-f, hollow spheres can be observed in both HCS-PA and HCS-A after heteroatom doping and secondary annealing at 900 ^{o}C under the protection of argon. For HCS-PA, PATI was carbonized and became large pieces of bulk carbon material, coexisting with nano spheres (Fig. 2c, d and Fig. S3). However, benefiting from the small molecular size of ATI, HCS-A largely retained the original spherical structure from HCS with granular additions, becoming nano-sized bumpy balls (Fig. 1 and Fig. S4d, inset). Also, as shown in the TEM images (Fig. 2f and Fig. S4), the surface of HCS-A is much smoother than that of activated HCS. This can be attributed to the ATI molecules adsorbing on the surface of activated HCS and filling the cavities of activated HCS. It was verified by N_2 adsorption-desorption isotherm BET surface area (Fig. S5 and Table S1) that HCS-A has a specific surface area of 1531 m^2 g^{-1}, which is less than that of activated HCS with a specific surface area of 2487 m^2 g^{-1}, illustrating that the surface area of activated HCS was partially covered by ATI. In comparison to HCS-PA (BET surface area of

987 m^2 g^{-1}), HCS-A shows much higher surface area because ATI is easier to volatize and decompose under high temperature than PATI, and ATI does not form large non-porous particles after high temperature treatment. During pyrolysis, the volatilization and decomposition of ATI could also help increase the porosity of HCS-A. However, for HCS-PA, the polymerization could cause both the formation of large particles and HCS agglomeration (Fig. 2c, d and Fig. S3), hence sacrificing most of the surface area.

As HCS-A and HCS-PA show different morphologies, it is important to study the final elemental composition and the chemical states of each element in these two catalysts. The X-ray photoelectron spectroscopy (XPS) survey scan (Fig. S6) indicates the existence of C, N, S, O and Fe elements after pyrolysis in both HCS-A and HCS-PA. The atomic ratios of nitrogen, sulfur and iron are shown in Fig. 3a. HSC-A shows lower nitrogen content than HCS-PA, indicating that more ATI moieties have volatilized and decomposed during pyrolysis. The bonding configurations of nitrogen in HCS-A and HCS-PA are shown by the N1s core level spectra (Fig. 3b). Both of the nitrogen spectra can be divided into three categories: pyridinic nitrogen (398.2 eV ± 0.2 eV), graphitic nitrogen (401.0 eV ± 0.2 eV), and oxidic nitrogen (404.0 eV ± 0.2 eV). Among these categories, pyridinic nitrogen and graphitic nitrogen are generally considered to be most active for ORR [23]. The peaks with lower binding energy, located at about 398.2 eV, can be attributed to pyridinic nitrogen, in which a pair of p-electrons appears in the π-conjugated system of the graphene layers. Pyridinic N is able to create a Lewis basic site, thus O_2 can be adsorbed at the carbon atom next to the pyridinic N. This is followed by protonation of the oxygen molecule and further reduction. When carbon atoms within the graphene layers are substituted by nitrogen atoms in the form of "graphitic" nitrogen, the corresponding peak in the high-resolution N1s spectra is located at 400.8eV. The high energy peak at 404.0 eV is

commonly attributed to the nitrogen oxide groups, which are considered inert in oxygen reduction reaction. Pyridinic nitrogen and graphitic nitrogen dominate in both HCS-A and HCS-PA. From the N1s peaks, we know quaternary N and pyridinic N are the dominating nitrogen species in both HCS-A and HCS-PA, which are likely to make the main contribution to the activity of the catalysts.

In addition to nitrogen, HCS-A and HCS-PA were simultaneously doped with sulfur as ATI and PATI contain both nitrogen and sulfur. The high-resolution S 2p spectra are shown in Fig. 3c, all of which came from the spin-orbit coupling, S $2p_{3/2}$ and S $2p_{1/2}$, with 1.2 eV energy splitting and 1:2 intensity ratio [24]. For both HCS-A and HCS-PA, the S 2p core level doublet centered at 163.8/165.0 shows the presence of C-S-C species [25], revealing successful S doping into the carbon matrix. The two minor doublets located between 161.4 to 163.8 eV are attributed to FeS_x species, indicating that a very small amount of S has combined with iron to form iron sulfides. Other minor doublets between 165.2 to 169.5 eV are attributed to SO_x species, which is reasonable as the activated HCS surface contains abundant oxygen containing groups after KOH activation (Table S2). The doublet centered at 163.8/165.0 accounts for 54% of the total S species, the majority of sulfur is doped into the carbon framework for both HCS-A and HCS-PA, and may positively modify the catalytic properties as reported by some other sulfur doped materials [26]. Sulfur doping could increase the spin density of the adjacent carbon atoms as well as the number of active atoms, which means that both activity and density of the active sites could be enhanced by sulfur doping. It also must be noted that although the activity of S-C moieties may be inferior to Fe-N moieties, the existence of S-C moieties broadens the potential range for oxygen reduction. In Fig. 3d, the XPS Fe 2p core level spectra show the same peak positions for HCS-A and HCS-PA. The Fe $2P_{3/2}$ peaks are located at 711.2 eV and Fe $2P_{1/2}$ peaks

are located at 724.1 eV, which are due to the coexistence of ferrous and ferric states [27]. Overall, it is very interesting to learn from the XPS spectra that independent of the precursors that have been used, the doped elements for HCS-A and HCS-PA appear in similar elemental composition and nearly identical chemical states for each element.

Energy dispersive X-ray spectroscopy (EDX) element mapping has been done to study the elemental distribution on the surface of HCS-A. Fig. 3f and g show that the mapping images of carbon and sulfur overlap with each other, indicating uniform S doping in the carbon matrix. The uniform sulfur distribution could benefit from the homogeneous absorption of ATI on HCS surface after mixing. Fig. 3h shows that parts of Fe elements gather together at certain spots where iron particles are located. Other than the iron particles, Fe atoms were also uniformly distributed on the HCS-A surface, which could be attributed to the effects of N and S tethering with Fe [28]. The distribution of iron elements can also be confirmed by electron energy loss spectroscopy (EELS) mapping in Fig. S7. Similar to the result obtained by EDX mapping, beside the agglomerated particles, iron was uniformly doped on the sphere surface.

Physicochemical characterization demonstrates that the catalysts prepared from ATI and PATI (i.e. HCS-A and HCS-PA) show similar elemental composition. Moreover, all the elements that closely relate to active sites (e.g. iron, nitrogen and sulfur) are almost of the same chemical states for the two materials, indicating that the same types of chemical bonds are formed among those elements within HCS-A and HCS-PA. Interestingly, HCS-A and HCS-PA show quite considerable differences in terms of morphology (Fig. 2c-f) and surface area (Fig. S5 and Table S1). HCS-A preserved the morphology of HCS with a few iron particles decorating on the sphere surface, while large (>500 nm) particles of carbon and small (~110 nm) spheres co-exist in HCS-PA. Accordingly, HCS-A inherited more of the surface area from activated HCS than HCS-PA

did. Structure and composition are the two key factors that affect activity, and any differences within these two factors could have an impact on the catalytic activity of HCS-A and HCS-PA.

3.2 Electrochemical Analysis

To evaluate the electrocatalytic ORR activity, linear sweep voltammetry (LSV) was carried out in both acidic (0.5 M H_2SO_4) and alkaline (0.1 M KOH) media. The catalysts were tested in both O_2 and N_2, and all the LSV curves for ORR were plotted after subtracting the N_2 background (Fig. 4a, b and Fig. S8). HCS-mf is a metal-free catalyst prepared from only HCS and aminothiophenol, with the same synthesis procedure as HCS-A. Both HCS-A and HCS-PA show much higher activities compared to the metal-free catalyst, testifying to the significance of the iron species to ORR activity. In acidic medium, HCS-A and HCS-PA reached the mass transport limiting current at a potential less than ca. 0.7 V vs. RHE. The mixed kinetic and mass transport controlled region was reached within the potential range from 0.7 V to 0.8 V vs. RHE. Both HCS-A and HCS-PA show higher activity in alkaline medium as seen in Fig. 4b. The mass transport limiting current was reached at around 0.8 V vs. RHE and the mixed control region is located between 0.8 V and 0.9 V vs. RHE. Compared to HCS-PA, HCS-A demonstrated superior ORR activity in both media in terms of half-wave potential and limiting current. At a current density of 2 mA cm^{-2}, HCS-A surpasses HCS-PA by 45 mV and 36 mV in 0.5 M H_2SO_4 and 0.1 M KOH, respectively (Table S3). Compared to other catalysts in literature, HCS-A achieved one of the best ORR activities reported so far, especially in alkaline medium (Table S4). HCS-A exhibited slightly lower onset potential than commercial TKK Pt/C catalyst in 0.1 M KOH, which means the active sites on HCS-A have intrinsically lower activity than Pt-based active sites. However, the half-wave potential of HCS-A is slightly higher than that of Pt/C catalyst. There are two main reasons for the higher half-wave potential: one is that the active sites on HCS-A are distributed more uniformly and closely, allowing for the involvement of more active

sites to facilitate the reaction, and thus current density is able increase faster at the kinetic region. The other reason is that the void spaces in HCS-A facilitated mass transport and made it easier and faster to reach the diffusion limiting current plateau. HCS-A shows a slightly higher limiting current density in both acid and base than HCS-PA, suggesting that the oxygen reduction pathways for HCS-A and HCS-PA could be slightly different in the two media. The overall multielectron reaction of oxygen reduction has two main pathways. One is a $2e^-$ reduction pathway which produces a peroxide species (HO_2^-), and the other is a direct $4e^-$ pathway which produces H_2O. The $2e^-$ transfer pathway can be represented as:

$O_2 + H^+ + 2e^- \rightarrow HO_2^-$ (Acidic medium) (1)

$O_2 + H_2O + 2e^- \rightarrow HO_2^- + OH^-$ (Alkaline medium) (2)

The direct $4e^-$ transfer pathway can be represented as:

$O_2 + 4H^+ + 4e^- \rightarrow 2H_2O$ (Acidic medium) (3)

$O_2 + 2H_2O + 4e^- \rightarrow 4OH^-$ (Alkaline medium) (4)

To clarify the reduction pathways for HCS-A and HCS-PA, we performed rotating ring disk electrode (RRDE) measurements to monitor the formation of peroxide species (HO_2^-) during the oxygen reduction process (Fig. 4 c, d and Fig. S9). The disk electrode was scanned catholically at a scanning rate of 5 mV s^{-1}, and the ring electrode was set at a 1.3 V vs. RHE to oxidize HO_2^-. The electron transfer number (n) and yield of peroxide species (%HO_2^-) was calculated by the following equation:

$$n = 4 \times \frac{I_d}{I_d + I_r/N} \quad (5)$$

$$HO_2^-\% = 200 \times \frac{I_r/N}{I_d + I_r/N} \quad (6)$$

In which I_d is the disk current, I_r is the ring current and N is the current collection efficiency of the ring electrode. N was determined to be 0.28 based on the reduction of $K_3Fe[CN]_6$. Since

oxygen can be either fully reduced to H_2O though the $4e^-$ pathway, or reduced to HO_2^- through the $2e^-$ pathway, the calculated electron transfer number is an apparent value which represents the mixture of the $2e^-$ and $4e^-$ pathways in a certain ratio. As observed in the figure, HCS-A shows a lower ring current density in both media (Fig. S9), meaning less HO_2^- was detected on the ring electrode. Electron transfer number and hydrogen peroxide production are also calculated and shown in Fig. 4c, d. Both HCS-A and HCS-PA show lower yields of HO_2^- in 0.1 M KOH, which is in well accordance with the polarization curve, demonstrating that both catalysts show higher activity in 0.1 M KOH. If we compare HCS-A and HCS-PA, it is easy to discover that HCS-A catalyzes the oxygen reduction with a higher electron transfer number in both media, which means HCS-A has better selectivity of the 4 e^- pathway to directly reduce O_2 to H_2O. A 4 e^- pathway is desired for the following two reasons: firstly, it brings higher cathode potential and helps increase the overall cell voltage; secondly, less HO_2^- being produced can reduce the attacks on the catalyst and increase the durability.

As discussed previously, ATI was uniformly distributed on the HCS surface, thus HCS-A has more homogeneously distributed active sites on its surface than HCS-PA. Additionally, HCS-A has a larger surface area, which allows for more accessible active sites. Therefore, even though HCS-A and HCS-PA show similarity in composition, the polarization curves start to differentiate from the kinetic region. In Fig. 4a, b (inset) we normalized current densities by the BET surface area of HCS-A and HCS-PA, respectively. It was found that, after normalization, the activity gap between these two catalysts are prominently reduced. It shows that catalytic activity is greatly affected by the surface area, which, in our case, is caused by the two different nitrogen precursors. However, because of the better active site distribution, HCS-A still shows slightly higher activity than HCS-A after normalization. Tafel slopes for HCS-A and HCS-PA in both

media are plotted to elucidate the reaction kinetics for ORR (Fig. 4e, f). A lower Tafel slope is desirable to drive a larger catalytic current density at a lower overpotential for a catalyst. As shown in the figures, Tafel slopes for HCS-A in acid and base are 63 mV/dec and 60 mV/dec, respectively. Comparing to the state of the art N-Fe-CNT/CNP catalyst reported in alkaline medium by Chung et al (-79 mV/dec) [29], HCS-A shows a lower Tafel slope in alkaline (-60 mV/dec), which means a faster reaction was obtained by HCS-A. As for HCS-PA, it has higher slopes (-74 mV/dec in 0.5 M H_2SO_4 and -69 mV/dec in 0.1M KOH) than HCS-A in both media, indicating a lower reaction rate than HCS-A in the kinetic region.

3.3 Durability and Methanol Tolerance Test

As HCS-A demonstrated optimal ORR activities in both media, it was selected for durability, methonal tolerance and full cell tests. To examine the durability of HCS-A, accelerated degradation testing (ADT) in the potential range of 0.6-1.0 V at a scan rate of 50 mV s^{-1} was performed for 10 thousand and 20 thousand cycles in acidic medium and alkaline medium, respectively. Fig. 5a shows the LSV curves for HCS-A before and after durability testing in acidic medium, demonstrating 34 mV downshift in half-wave potential with no notable change on the mass transport limiting current. LSV curves for HCS-A before and after durability testing in the alkaline medium is shown in Fig. 5b. HCS-A only dropped 2 mV on its half-wave potential after 20000 cycles, which is, to our knowledge, one of the lowest activity loss (after 20000 durability cycles) reported so far.

The sample after durability testing was collected from the electrode to study its morphological transformation. The TEM images for HCS-A after ADT in both acidic and alkaline media was shown in Fig. 5c, d. It was discovered that HCS-A was able to preserve the hollow spherical structure in both media, which is reasonable since carbon was found to be relatively stable under

the oxidation potential of 1.0 V vs. RHE. However, HCS-A after ADT in acid medium does not retain the iron particles that was decorated on its surface. Since the iron particles can synergistically catalyze the oxygen reduction process, the dissolution of iron particles in acidic medium could be one of the reasons for HCS-A activity degradation. Another reason which could have caused the catalyst's activity to decline is the protonation of the nitrogen atoms in the active sites. The protonation introduces subsequent anion adsorption on the protonated nitrogen and leads to ultimate deactivation of the active sites [31]. Also, as detected by RRDE, HCS-A has an H_2O_2 yield of 5% in the acidic medium. The H_2O_2 formed by the incomplete reduction of O_2 could result in the formation of hydroxyl free radicals (·OH) under the promotion of Fe^{2+} following the reaction [32]:

$$Fe^{2+} + H_2O_2 + H^+ = Fe^{3+} + \cdot OH + H_2O \quad (7)$$

Both H_2O_2 and ·OH were able to attack active sites and caused activity loss. Unlike in acidic medium, HCS-A after ADT in alkaline medium does not show considerable differences in morphology compared to the original material. The outstanding durability that HCS-A show in alkaline medium in contrast to the relatively poor durability in acidic medium can be attributed to three reasons. Firstly, the iron particles were more stable under alkaline conditions and were well preserved during the test. Secondly, protonation of active sites was greatly inhibited due to the lack of protons in the alkaline electrolyte. At last, H_2O_2 yield was much lower in alkaline, and its transformation to ·OH was even less likely to took place without H^+.

It is well known that Pt-based catalyst can be poisoned by methanol, hindering its application in the cathode of direct methanol fuel cells (DMFCs). That is because platinum has a propensity to adsorb methanol and oxidize it to carbon monoxide (CO), in which the oxidation process simultaneously takes place with oxygen reduction [33], thus reducing the cell voltage. Moreover,

the CO by-product can poison the catalyst by occupying the Pt surface. In this work, we further studied the methanol tolerance ability of HCS-A by chronoamperometric measurements. As observed in Fig. 6a for the acidic medium, the ORR current at 0.6 V vs. RHE does not show much difference after methanol was added to the electrolyte at 2000 s, to a resulting methanol concentration of 3 M. In contrast, commercial Pt/C catalyst shows significant activity drop as its ORR current has endured a current loss of ca. 60% after methanol was added to the solution. In alkline medium (Fig. 6b), after methanol was added to the electrolyte, Pt/C shows dramatic current drop to a value around zero and slowly recover to ca. 40% of its original current. On the other hand, HCS-A maintained its current and was barely influenced by the methanol.

3.4 Full Cell Test

To further verify the ORR activity for HCS-A, fuel cell tests were performed in a single cell using a condition-controlled fuel cell test station (Scribner 850e). A set of membrane electrode assembly (MEA, top left), single cell (top right) and testing system (bottom) used in our work is shown in Fig. 7a to exemplify the experiments. The schematic in Fig. 7b illustrates the fuel cell working mechanism with HCS-A as the cathode catalyst. A maximum fuel cell power density of 500 mW cm^{-2} was obtained in a single cell test (Fig. 7c), which is quite a decent performance for non-precious metal catalyst supported PEM fuel cells. For the testing in alkaline medium, a home-made zinc-air battery was designed to test ORR activity of HCS-A. Fig. 7d shows the gas diffusion layer sprayed with a layer of HCS-A (top figure) and the assembled zinc-air battery cell (bottom figures). The zinc-air working mechanism with HCS-A as the cathode catalyst is illustrated in Fig. 7e. In our experiment, to simulate a real operating condition, the zinc-air battery was tested in ambient air with no O_2 pre-bubbling or continuous O_2 flow. The battery

reached a maximum discharge power density of 195 mW cm^{-2} (Fig. 7f), which is among the best zinc-air performances obtained in ambient air to date (Table S5).

4. CONCLUSION

In this paper, we have designed an ultra-high surface area hollow carbon sphere (HCS). With this HCS as the carbon support, two types of heteroatom doped catalyst HCS-PA and HCS-A were prepared with aminothiophenol and poly-aminothiophenol, respectively, as the doping agent. It was manifested that both of these, monomer and polymer, acting as heteroatom doping precursors, were able to increase ORR activity. However, the monomer, aminothiophenol, could be a better choice to obtain favourable morphology and surface area retention of the ultra-high surface area spherical supporting material. With the obtained unique embellished hollow sphere structure and high surface area, HCS-A showed remarkable ORR activity in both acidic and alkaline media. In addition to outstanding ORR activity, HCS-A also demonstrated excellent durability with negligible degradation after 20000 cycles in alkaline medium. PEM fuel cell test with HCS-A as a cathode catalyst reached a peak power density of 500 mW cm^{-2}. In a zinc-air battery test, the discharging power density of HCS-A reached a maximum of 195 mW cm^{-2} in ambient air, which is one of the best zinc-air performances reported in ambient conditions. Our study not only reports a catalyst with high activity but more importantly validates a strategy to maintain the structural advantages from a favorable supporting material.

ACKNOWLEDGMENTS

This work was supported by the University of Waterloo, the Waterloo Institute for Nanotechnology and Ballard Power Systems. This research was conducted as part of the

Catalysis Research for Polymer Electrolyte Fuel Cells (CaRPE-FC) network administered from Simon Fraser University and supported by Automotive Partnership Canada (APC) Grant no. APCPJ 417858-11 through the Natural Sciences and Engineering Research Council of Canada (NSERC).

REFERENCES

[1] X. Fu, F. M. Hassan, P. Zamani, G. Jiang, D. C. Higgins, J.-Y. Choi, X. Wang, P. Xu, Y. Liu and Z. Chen, Nano Energy 42 (2017) 249-256.
[2] E. M. Erickson, C. Ghanty and D. Aurbach, J. Phys. Chem. Lett. 5 (2014) 3313-3324.
[3] J. Wang, H. Wu, D. Gao, S. Miao, G. Wang and X. Bao, Nano Energy 13 (2015) 387-396.
[4] W. Xue, Q.-B. Yan, G. Xu, L. Suo, Y. Chen, C. Wang, C.-A. Wang and J. Li, Nano Energy 38 (2017) 12-18.
[5] C. Ding, H. Zhang, X. Li, T. Liu and F. Xing, J. Phys. Chem. Lett. 4 (2013) 1281-1294.
[6] Y. Nie, L. Li and Z. Wei, Chem. Soc. Rev. 44 (2015) 2168-2201.
[7] U. I. Kramm, J. Herranz, N. Larouche, T. M. Arruda, M. Lefevre, F. Jaouen, P. Bogdanoff, S. Fiechter, I. Abs-Wurmbach, S. Mukerjee and J.-P. Dodelet, Phys. Chem. Chem. Phys. 14 (2012) 11673-11688.
[8] U. I. Koslowski, I. Abs-Wurmbach, S. Fiechter and P. Bogdanoff, J. Phys. Chem. C 112 (2008) 15356-15366.
[9] J. Tian, A. Morozan, M. T. Sougrati, M. Lefèvre, R. Chenitz, J. P. Dodelet, D. Jones and F. Jaouen, Angew. Chem. Int. Ed. 125 (2013) 7005-7008.
[10] L. Qu, Y. Liu, J.-B. Baek and L. Dai, ACS nano 4 (2010) 1321-1326.
[11] P. H. Matter, L. Zhang and U. S. Ozkan, J. Catal. 239 (2006) 83-96.
[12] R. Jasinski, J. Electrochem. Soc. 112 (1965) 526-528.
[13] S. Gupta, D. Tryk, I. Bae, W. Aldred and E. Yeager, J. Appl. Electrochem.19 (1989) 19-27.
[14] M.-Q. Wang, W.-H. Yang, H.-H. Wang, C. Chen, Z.-Y. Zhou and S.-G. Sun, ACS Catal. 4 (2014) 3928-3936.
[15] Y. Ye, H. Li, F. Cai, C. Yan, R. Si, S. Miao, Y. Li, G. Wang and X. Bao, ACS Catal., DOI: 10.1021/acscatal.7b02101 (2017) 7638-7646.
[16] Y. Zhao, K. Watanabe and K. Hashimoto, J. Am. Chem. Soc. 134 (2012) 19528-19531.
[17] Z. Lu, J. Wang, S. Huang, Y. Hou, Y. Li, Y. Zhao, S. Mu, J. Zhang and Y. Zhao, Nano Energy 42 (2017) 334-340.
[18] S. Gao, L. Li, K. Geng, X. Wei and S. Zhang, Nano Energy 16 (2015) 408-418.
[19] J. Liang, Y. Jiao, M. Jaroniec and S. Z. Qiao, Angew. Chem. Int. Ed. International Edition 51 (2012) 11496-11500.
[20] C. Zhou, J. Han, G. Song and R. Guo, J. Polym. Sci. A 46 (2008) 3563-3572.
[21] S. Ikeda, S. Ishino, T. Harada, N. Okamoto, T. Sakata, H. Mori, S. Kuwabata, T. Torimoto and M. Matsumura, Angew. Chem. Int. Ed. 118 (2006) 7221-7224.

[22] M. Sevilla and R. Mokaya, Energy Environ. Sci. 7 (2014) 1250-1280.
[23] C. Zhang, R. Hao, H. Liao and Y. Hou, Nano Energy 2 (2013) 88-97.
[24] Z. Wang, Y. Dong, H. Li, Z. Zhao, H. B. Wu, C. Hao, S. Liu, J. Qiu and X. W. D. Lou, Nat. Commun. 5 (2014) 5002.
[25] P. Ganesan, M. Prabu, J. Sanetuntikul and S. Shanmugam, ACS Catal. 5 (2015) 3625-3637.
[26] M. Ferrandon, A. J. Kropf, D. J. Myers, K. Artyushkova, U. Kramm, P. Bogdanoff, G. Wu, C. M. Johnston and P. Zelenay, J. Phys. Chem. C 116 (2012) 16001-16013.
[27] L. Lin, Q. Zhu and A.-W. Xu, J. Am. Chem. Soc. 136 (2014) 11027-11033.
[28] R. Cao, R. Thapa, H. Kim, X. Xu, M. Gyu Kim, Q. Li, N. Park, M. Liu and J. Cho, Nat. Commun. 4 (2013) 2076.
[29] H. T. Chung, J. H. Won and P. Zelenay, Nat. Commun. 4 (2013) 1922.
[30] K. Wan, Z.-p. Yu, X.-h. Li, M.-y. Liu, G. Yang, J.-h. Piao and Z.-x. Liang, ACS Catal. 5 (2015) 4325-4332.
[31] J. Herranz, F. Jaouen, M. Lefèvre, U. I. Kramm, E. Proietti, J.-P. Dodelet, P. Bogdanoff, S. Fiechter, I. Abs-Wurmbach, P. Bertrand, T. M. Arruda and S. Mukerjee, J. Phys. Chem. C 115 (2011) 16087-16097.
[32] L. Gubler, S. M. Dockheer and W. H. Koppenol, J. Electrochem. Soc. 158 (2011) B755-B769.
[33] E. Antolini, T. Lopes and E. R. Gonzalez, J. Alloy. Comp. 461 (2008) 253-262.

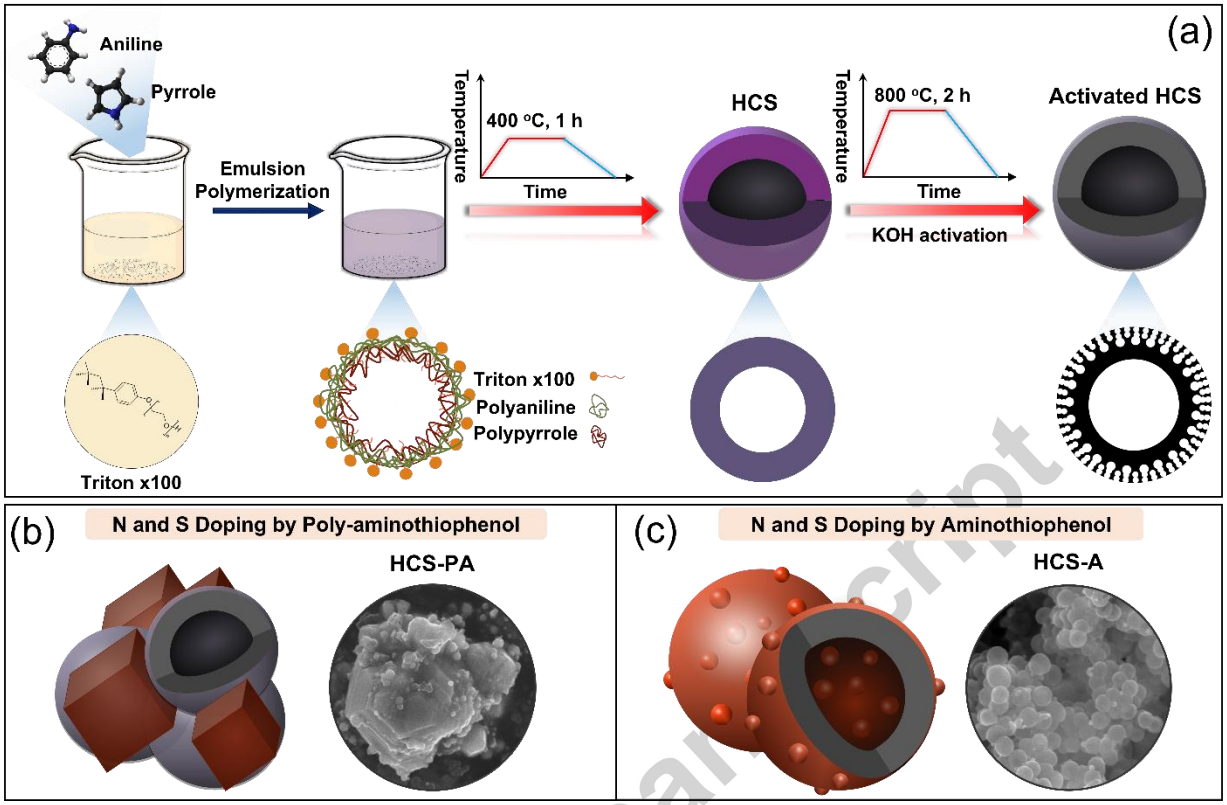

Fig. 1. Synthesis process of a) Activated HCS, b) HCS-PA and c) HCS-A.

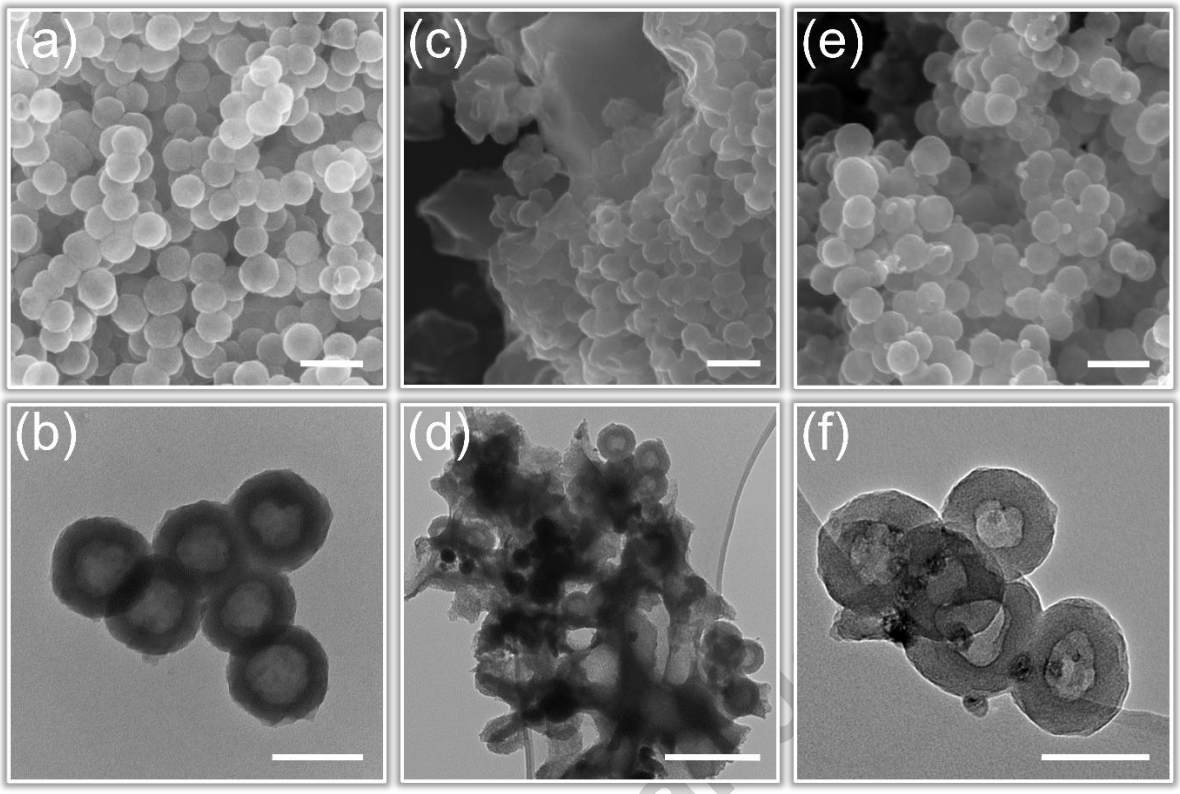

Fig. 2. SEM images of a) HCS, c) HCS-PA, e) HCS-A, and TEM images of b) HCS, d) HCS-PA, f) HCS-A. Scale bar: a, c) 200 nm, d, e) 300 nm and b, f) 100 nm.

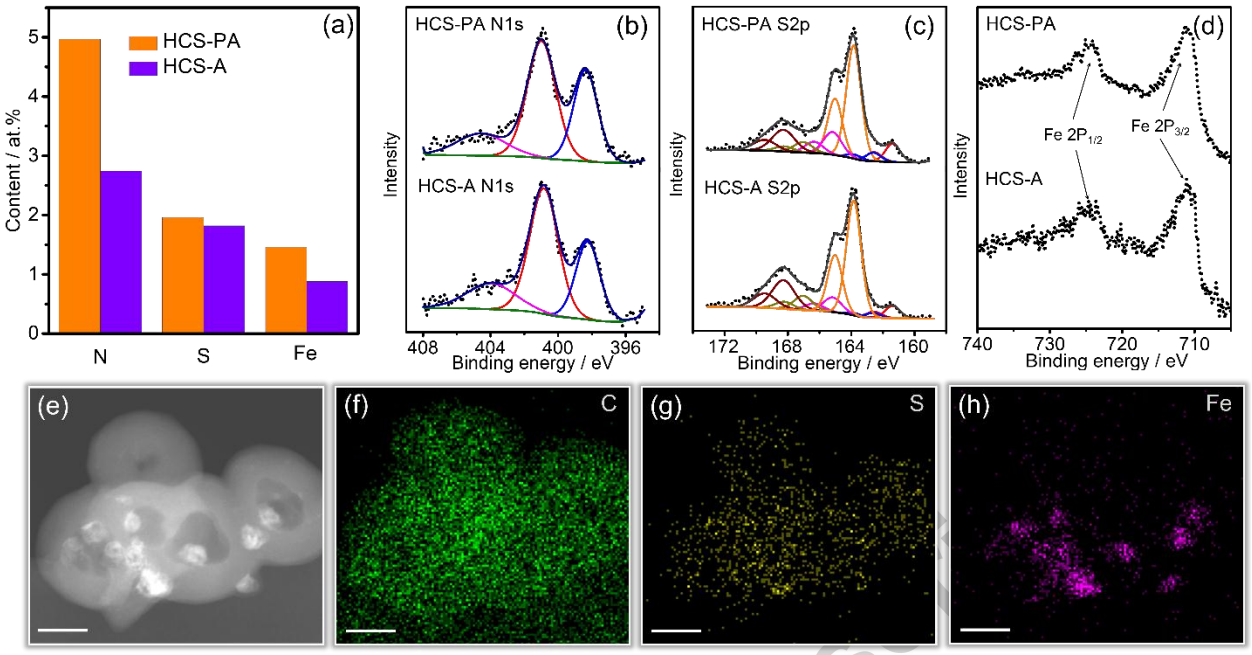

Fig. 3. Elemental analysis of HCS-PA and HCS-A. a) N 1s, b) S 2p and c) Fe 2P XPS spectra, d) N, S and Fe content. e-h) STEM dark field image and the corresponding EDX element mapping for the C, S and Fe atoms for HCS-A, Scale bar: 50 nm.

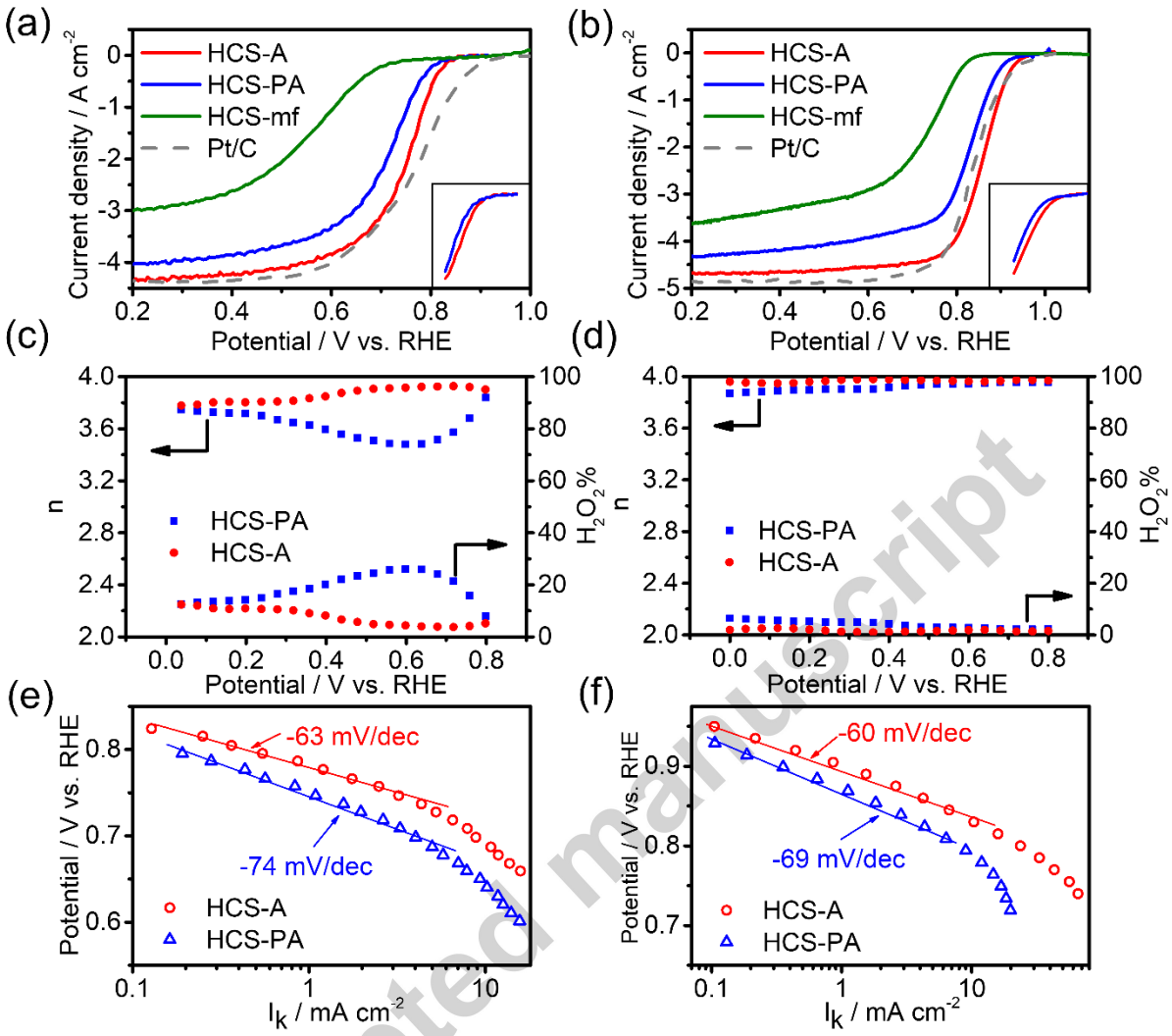

Fig. 4. RDE polarization curves of HCS-A, HCS-PA, HCS-mf and Pt/C in a) 0.5 M H_2SO_4 and b) 0.1 M KOH, a) and b) inset, LSV curves of HCS-A and HCS-PA, at the kinetic region, normalized by the BET surface area, rotating speed: 900 rpm, scanning rate: 5 mV cm^{-2}. Electron transfer number and peroxide species yield calculated for HCS-A and HCS-PA in c) 0.5 M H_2SO_4 and d) 0.1 M KOH. Tafel plots calculated for HCS-A and HCS-PA in e) 0.5 M H_2SO_4 and f) 0.1 M KOH.

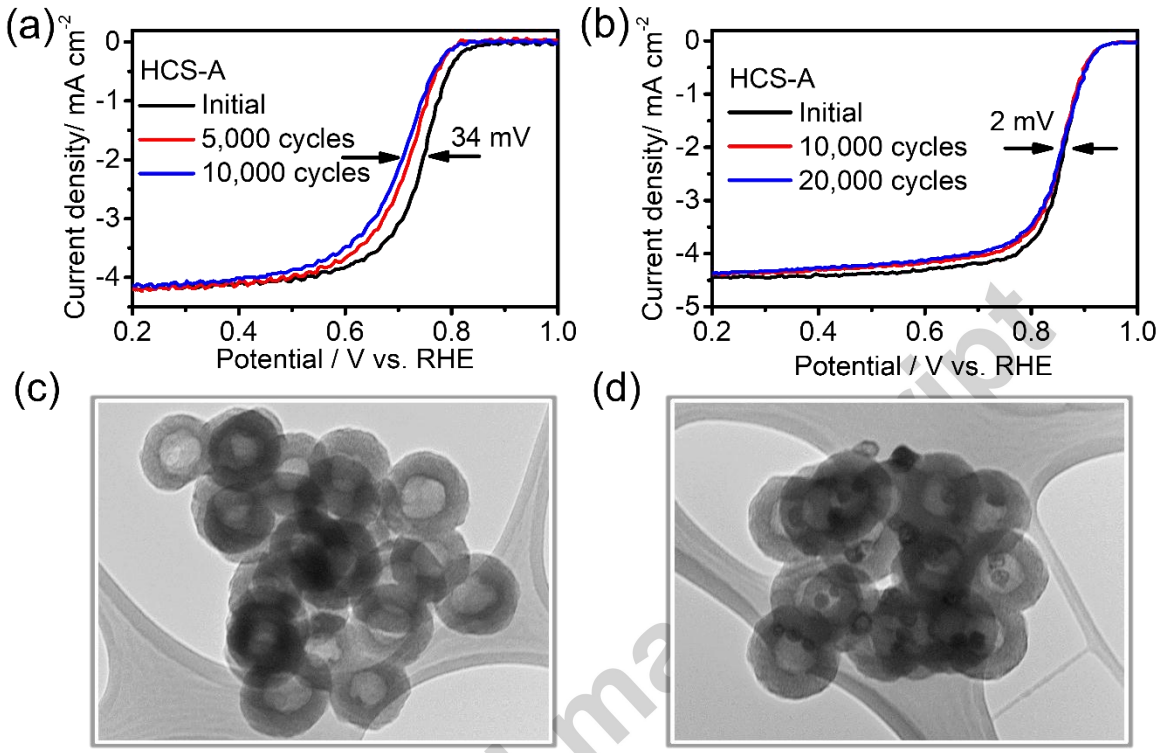

Fig. 5. LSV curves for HCS-A before and after cycling durability test in a) 0.5 M H_2SO_4 and b) 0.1 M KOH. TEM images of HCS-A after ADT in c) 0.5 M H_2SO_4, and d) 0.1 M KOH. Scale bar: 100 nm.

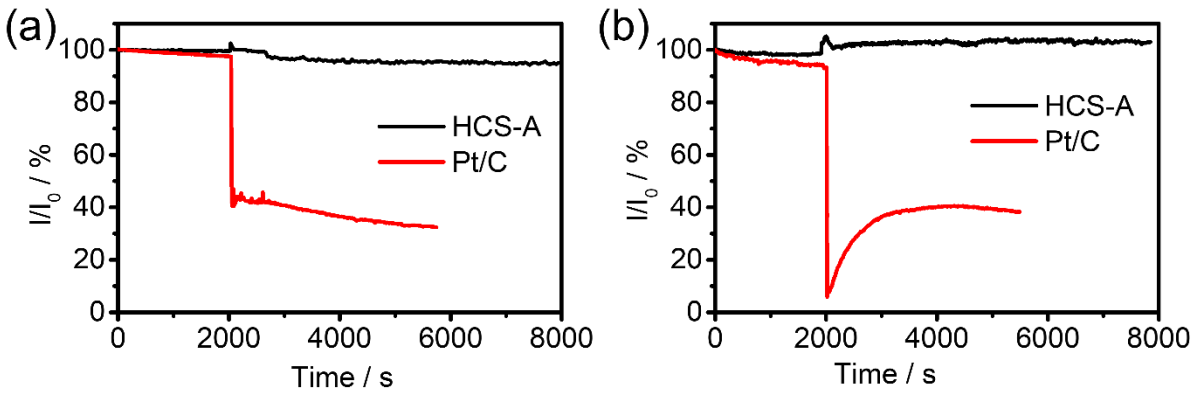

Fig. 6. Chronoamperometric responses for the HCS-A catalyst and commercial TKK 46.6 wt% Pt/C catalyst obtained at 0.6 V vs. RHE in a) 0.5 M H_2SO_4 and b) 0.1 M KOH with addition of methanol (resulting concentration of 3 M) at 2000 s.

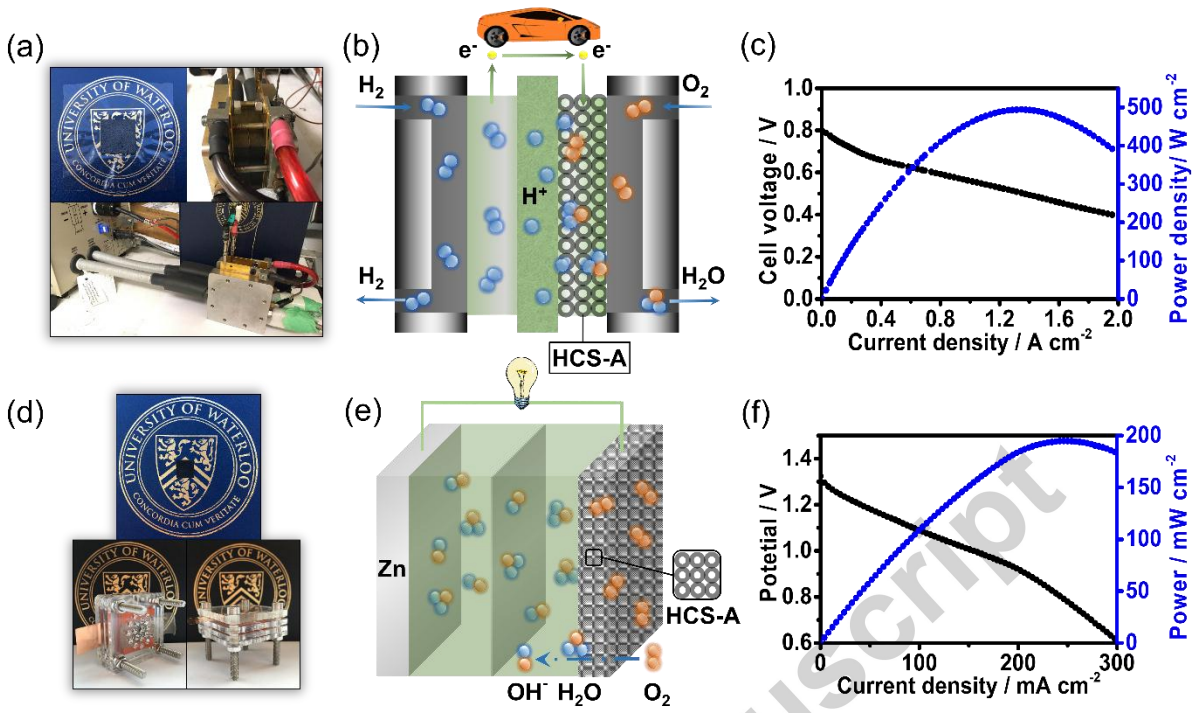

Fig. 7. Photograph of a) fuel cell and d) homemade zinc-air battery. Schematic illustration of b) fuel cell and e) zinc-air battery. Cell voltage and power density plots with HCS-A cathode for c) H_2-O_2 fuel cells and f) zinc-air battery in ambient air.

Highlights:

1. Monomer and polymer was compared to elucidate the selection of nitrogen precursor;

2. Longest half-cell durability to date was achieved in alkline medium;

3. One of the highest peak power density was achieved in ambient zinc-air battery.